Nature Communications

https://doi.org/10.1038/s41467-026-71165-w

Article in Press

A lightweight zero thermal expansion magnesium alloy

Received: 23 June 2025

Accepted: 13 March 2026

Cite this article as: Huang, Y., Wu, S., Dong, Z. *et al.* A lightweight zero thermal expansion magnesium alloy. *Nat Commun* (2026). https://doi.org/10.1038/s41467-026-71165-w

Yadong Huang, Sujuan Wu, Zhihua Dong, Jiangfeng Song, Guilin Wu, Cong Wang, Shengwen Bai, Pascal Brault, Bin Jiang & Fusheng Pan

We are providing an unedited version of this manuscript to give early access to its findings. Before final publication, the manuscript will undergo further editing. Please note there may be errors present which affect the content, and all legal disclaimers apply.

If this paper is publishing under a Transparent Peer Review model then Peer Review reports will publish with the final article.

ARTICLE IN PRESS

© The Author(s) 2026. **Open Access** This article is licensed under a Creative Commons Attribution-NonCommercial-NoDerivatives 4.0 International License, which permits any non-commercial use, sharing, distribution and reproduction in any medium or format, as long as you give appropriate credit to the original author(s) and the source, provide a link to the Creative Commons licence, and indicate if you modified the licensed material. You do not have permission under this licence to share adapted material derived from this article or parts of it. The images or other third party material in this article are included in the article's Creative Commons licence, unless indicated otherwise in a credit line to the material. If material is not included in the article's Creative Commons licence and your intended use is not permitted by statutory regulation or exceeds the permitted use, you will need to obtain permission directly from the copyright holder. To view a copy of this licence, visit http://creativecommons.org/licenses/by-nc-nd/4.0/.

A lightweight zero thermal expansion magnesium alloy

Yadong Huang[a,b†], Sujuan Wu[a,b,c,*,†], Zhihua Dong[a,b], Jiangfeng Song[a,b], Guilin Wu[a,d,*], Cong Wang[e], Shengwen Bai[a,b], Pascal Brault[f], Bin Jiang[a,b,c*], Fusheng Pan[a,b,c]

a. College of Materials Science and Engineering, Chongqing University, Chongqing 400044, China

b. National Engineering Research Center for Magnesium Alloys, Chongqing University, Chongqing 400044, China

c. Institute of Lightweight Materials and Engineering, Mingyue Lake Laboratory, 401122, Chongqing, China

d. International Joint Laboratory for Light Alloys (MOE), College of Materials Science and Engineering, Chongqing University, Chongqing 400044, China

e. School of Integrated Circuit Science and Engineering, Beihang University, Beijing 100191, China

f. GREMI, CNRS, Université d'Orléans, 14 rue d'Issoudun, F-45067 ORLEANS, France

[†] Equally contributing
* Corresponding authors
Email: sujuan.wu@cqu.edu.cn; wugl@cqu.edu.cn; jiangbinrong@cqu.edu.cn

Abstract

Thermal expansion is an intrinsic property of metals and alloys, posing a critical challenge for achieving dimensional stability in lightweight systems where low atomic mass enhances lattice vibrations. Here we present a strain recovery compensation strategy that achieves three orders of magnitude reduction in thermally induced volume change, enabling zero thermal expansion (ZTE) in a rare-earth magnesium alloy containing 1.2 *vol*.% Al-stabilized MnCoGe particles. The coefficient of thermal expansion is reduced from 28×10^{-6} °C^{-1} to 0.02×10^{-6} °C^{-1} over 25–150 °C—the highest thermal stability reported for any alloy. This alloy also retains high compressive strength (424 MPa), ductility (12%), and ultralow density (1.93 g/cm^3). The ZTE behavior arises from sustained compressive strain, maintained by reversible martensitic transformation of the embedded particles. Beyond realizing a dimensional stable lightweight alloy, this work establishes a generalizable principle for achieving thermal dimensional stability in metals via recoverable strain.

Introduction

Thermal dimensional stability is critical for structural reliability in systems exposed to temperature fluctuations, such as aerospace, cryogenics, precision instrumentation, and microelectronics manufacturing[1–4]. Yet all metals expand upon heating due to anharmonic atomic vibrations, quantified by the coefficient of thermal expansion (CTE)[5]. This behavior poses a persistent challenge in maintaining dimensional accuracy under thermal cycling. One notable exception is Invar alloy ($Fe_{65}Ni_{35}$), recognized with a Nobel Prize in Physics for achievement zero thermal expansion (ZTE; CTE $\leq 1.5 \times 10^{-6}$ °C^{-1}) between –60 °C and 80 °C due to magnetically driven volume changes[6,7]. However, such magneto-volume coupling is limited to specific magnetic alloys and is not applicable to lightweight, non-magnetic metals like magnesium and aluminum, which are increasingly vital in transportation and aerospace[8,9]. Achieving ZTE in these systems remains an unresolved challenge.

Macroscopic thermal expansion reflects cumulative atomic displacements with temperature, typically measured via changes in length, volume, or pressure dependent entropy at fixed temperature[10,11]. In metals and alloys, plastic deformation accommodates amounts of defects and residual strains, displacing atoms from their equilibrium lattice sites[12,13]. Upon heating, defect migration and interaction can partially relieve these internal strains, reducing the net dimensional change[14,15]. This defect mediated strain recovery alters both volumetric and entropic responses[16–19], and thereby causing the CTE to be governed by the competition between thermally induced atomic displacements and their reduction via preserved strain recovery[14,20,21]. However, the complex, nonlinear nature of defect dynamics in strain recovery makes their impact on macroscopic CTE or thermal stability still elusive.

In this work, we propose that ZTE can emerge when strain contraction precisely offsets thermal expansion and sustaining this dynamic balance during continuous heating enables ZTE over a broader temperature range (Figure 1a). Unlike conventional models that treat thermal expansion as a purely elastic lattice response[22,23], the inherent plastic deformation capabilities of metals and alloys allow them to maintain this balance over broader thermal intervals. However, strain recovery is irreversible-once released upon heating, it cannot spontaneously regenerate[24]. Herein, we introduce a sustainable strain generation strategy, achieved through engineered martensitic transformations within a soft metallic matrix, establishing a sustainable and generalizable pathway to achieve and maintain ZTE across extended temperature ranges. We demonstrate this design strategy in a Mg alloy (WE43: Mg–4Y–3.3RE (Nd, Gd)–0.5Zr, *wt*.%) by incorporating 1.2 *vol*.% Al-stabilized MnCoGe particles. MnCoGe undergoes a martensitic transformation near 150 °C, producing a ~4% volume change[25–27]. The hexagonal close-packed (HCP) structure of Mg provides high-temperature plasticity but retains substantial residual strain upon cooling due to limited slip systems[28]. A remarkable elastic modulus mismatch between MnCoGe (164 GPa)[29] and the Mg matrix (45 GPa)[30] promotes plastic deformation in the matrix during transformation, thereby generating significant strain. An Al-enriched gradient layer, formed via Al diffusion on MnCoGe particles (Supplementary Figures 16, 17), stabilizes their reversible martensitic transition.

Results and Discussion

Modulating thermal expansion behavior by strain introduction

We compare WE43 alloys with and without MnCoGe to probe the strain distribution (Figures 1b-e) by electron backscatter diffraction (EBSD). The baseline alloy exhibits uniform grains and lacks pronounced crystallographic texture, indicating minimal residual strain at room temperature. The kernel average misorientation (KAM) analysis demonstrate that MnCoGe-containing alloys display refined grains and elevated geometrically necessary dislocation (GND) density (Figures 1c, 1e), reflecting enhanced strain retention. High-resolution transmission microscopy (HRTEM) further confirms dense dislocation networks (Figure 1f) and localized lattice distortion near interfaces of particle and matrix (Figure 1g). A few-layer non-coherent interface concentrates local strain and enables efficient transfer of thermal mismatch stress between the particle and the Mg matrix (Supplementary Figure 18). Lattice parameter measurements further reveal compression strains near MnCoGe particles relative to the bulk matrix.

We evaluated the CTE and mechanical performance of the designed Mg alloys (Figures 2a, 2b, Supplementary Figure 3). The alloy containing 1.2 *vol.*% Al-stabilized MnCoGe particles exhibits ZTE, with an ultralow CTE of 0.02×10^{-6} °C^{-1} maintained over 25°C to 150 °C. This value represents a three order of magnitude decrement compared to the pure WE43 alloy, and a temperature window of 125 °C. Notably, the CTE value is two orders of magnitude lower than that of Invar alloys, representing a significant enhancement in thermal dimensional stability. After three thermal cycles under a constant heating/cooling rate of 5 °C min^{-1}, the CTE stabilizes at ~0.2×10^{-6} °C^{-1} (Figure 2c), indicating the establishment of a steady balance between strain recovery and thermal expansion following the relaxation of fabrication induced residual strain.

The incorporation of MnCoGe particles simultaneously enhances the mechanical performance. The ultimate compressive strength increases from 384 to 424 MPa, while ductility remains at ~12%. This strain compensation approach enables the creation of an ultralight ZTE alloy (1.93 g/cm^3), uniquely combining high strength, ductility, and thermal dimensional stability. Comparative analyses with previously reported ZTE materials[31–42] reveal that this alloy has the lowest absolute CTE value reported to date (Figure 2d), an order of magnitude lower than most near-zero-expansion materials, along with a broad ZTE window (~25–150 °C) that far exceeds the effective temperature ranges of conventional Invar alloys and brittle oxide- or intermetallic-based ZTE materials. This temperature range coincides with the operational conditions of aerospace structural components, satellite optical benches, precision actuators, electronic and battery housings, and optical instrument bases, where repeated thermal cycling can induce dimensional drift and compromise alignment or functional accuracy. As a lightest (Figure 2e) ZTE alloy, it offers superior dimensional stability, high processing adaptability, and mechanical robustness, overcoming the limitations of conventional composites or Invar-type alloys. Collectively, these properties render the 1.2 *vol.*% Al-stabilized MnCoGe/Mg alloy a suitable candidate for applications requiring both lightweight design and reliable thermal stability under realistic service conditions.

Tracking the Evolution of Strain

Crucially, the regeneration of the strain upon cooling, driven by reversible martensitic transformation in MnCoGe, sustains the dynamic equilibrium between thermal expansion and strain contraction. To directly observe this process, we tracked strain evolution in the Mg matrix using in situ EBSD during thermal cycling (Figure 3a). At room temperature, grains near MnCoGe particles display significant inter- and intra-granular strain, reflected by color variations in orientation and misorientation maps (Supplementary Figures 4, 5). KAM mapping reveals a progressive strain reduction with heating, where highly strained regions nearly vanish above the martensitic transformation temperature (Figure 3b). Notably, strain reappears upon cooling, further confirmed by the density of GND, which decreases with increasing temperature and reaccumulates upon cooling (Figure 3c, Supplementary Figure 6).

In-situ HRTEM observations at the nanoscale show temperature driven dislocation motion, annihilation, and redistribution near MnCoGe interfaces (Supplementary Figure 7). Strain recovery is evidenced not only by changes in dislocation density but also by grain rotation (Supplementary Figure 8), suggesting multiple pathways for strain relaxation and regeneration. Subsequently, the variation of strain energy[43] across different temperatures was calculated (Figure 3d). The results show a continuous decrease during heating and restoration upon cooling, aligning with the mesoscopic trends observed. High-resolution TEM (Supplementary Figure 10) reveals that the dislocation networks are dominated by mobile <a> dislocations gliding on basal planes, consistent with the critical resolved shear stress hierarchy in HCP Mg. The cyclic recovery (Figures 3b-d) thus arises from the reversible glide and rearrangement of <a> dislocations, enabling temporary strain storage and release.

In situ X-ray diffraction (XRD) analysis further confirms lattice strain variation in thermal cycling. The Mg matrix exhibits peak shifts toward lower diffraction angles during heating, indicating strain relaxation (Figure 3e, Supplementary Figure 9). Upon cooling, peaks shift back, reflecting strain reintroduction. Quantitative analysis using the Williamson–Hall (WH) method[44] indicates that compressive strains are progressively alleviated during heating, reaching a minimum near 200 °C, and are reinstated upon cooling (Figure 3f).

Collectively, these multiscale observations demonstrate a dynamic strain self-compensation process that dislocation mediated relaxation and lattice recovery dominate during heating, while existence of MnCoGe induced stresses restore strain during cooling. This cyclic strain evolution stabilizes macroscopic dimensions across thermal cycles, thus underpinning the observed sustainable ZTE behavior.

Strain recovery on thermal expansion

To elucidate the thermodynamic basis of strain recovery induced ZTE, we performed differential scanning calorimetry (DSC) to track phase transition energetics in the MnCoGe-containing alloy. Unlike conventional systems, where accumulated matrix strain energy is irreversibly dissipated upon heating and cannot regenerate upon cooling, our ZTE alloy exhibits a distinct exothermic peak during cooling (Figure 4a)—absent in the pure WE43 matrix. The enthalpy of this exothermic event exceeds that of intrinsic MnCoGe martensitic transformation[45] (Figure 4b, Supplementary Figure 11), indicating additional energy contributions beyond the phase change alone. We attribute this anomalous thermal response to constrained interfacial deformation arising from thermal expansion mismatch between the Mg matrix and MnCoGe particles. This mismatch preserves residual elastic strain energy[46–48] during heating in Mg matrix, which is partially released upon reverse transformation during cooling. The synergistic interplay between strain coupling and phase transformation thermodynamics enables a sustainable ZTE behavior, extending the operational temperature window far beyond that of the intrinsic transformation of MnCoGe.

Classical thermoelastic modeling predicts that 1.2 *vol*. % MnCoGe can generate cooling induced internal stresses of ~ 140 MPa (Supplementary Figures 2, 12), exceeding the yield strength of the Mg matrix and inducing plastic deformation across ~30 *vol.*% of the matrix. Crystal Plastic Finite Element simulations further show increasingly heterogeneous strain fields and elastic strain-energy densities with larger or closely spaced particles

(Supplementary Figure 15). Such strain region includes anisotropic compressive or tensile stresses along the c-axis or the a/b-axes, allowing for the quantification of associated lattice volume changes (Figure 4c). To resolve how these strain states evolve with temperature, we analyzed their corresponding changes of statistical probabilities. In the undeformed alloy, strain state probabilities increase with temperature. In contrast, deformed Mg exhibits a reduction of probabilities in both compressive and tensile strain states during heating, consistent with strain recovery via defect migration and annihilation (Figure 4d).

Importantly, the recovery of compressive strain in ~30 *vol*. % of the Mg matrix induces a net negative thermal expansion of -0.17×10^{-6} °C^{-1} over 25 to 150 °C (Figure 4e, details in Supplementary Note2). A comparative analysis between fully compressive and tensile strain states highlights the dominant role of compressive strain recovery in enabling the observed ZTE behavior. Notably, this mechanism is generalizable in Al alloys incorporating MnCoGe, where the CTE also markedly decreases below the transformation temperature (Supplementary Figure 13). These findings establish strain recovery driven compensation as a universal strategy to achieve thermal dimensional stability in lightweight alloys system.

Above all, this strain recovery strategy provides an effective approach to maintain thermal dimensional stability in lightweight alloys. By quantitatively tracking the statistical evolution of local strain states, we also establish an interpretive framework linking plastic strain recovery to macroscopic thermal expansion. This perspective redefines the thermomechanical design rules for achieving ZTE, extending beyond traditional Invar-type magneto-volume mechanisms. Our findings introduce a paradigm for designing lightweight and ductile ZTE alloys with broad operating temperature windows, while also advancing fundamental understanding of the interplay between plasticity, phase transformation, and thermal stability in metallic systems.

Methods

Sample preparation

Equivalent amounts of Mn, Co, and Ge metals were mixed and melted four times in a vacuum furnace. After natural cooling to room temperature, the samples were collected and ground into powder using a planetary ball mill at 250 r/min for 5 hours. MnCoGe particles with different mass ratios, Al powder and WE43 powder were mixed with a planetary ball mill at 80 r/min for 2.5 h. The mixtures were then loaded into a graphite mold and sintered in a vacuum hot-press furnace under the following conditions: a vacuum of 1×10^{-5} Pa, a pressure of 20 MPa, a temperature of 550 °C, and a dwelling time of 1 hour. The samples were then cooled to room temperature. For comparison, reference samples of pure WE43 and WE43 with only MnCoGe particles added were also prepared under identical conditions.

Microstructure characterization

EBSD measurements were performed on a field-emission scanning electron microscope (JEOL JSM-7800F) equipped with an Oxford Instruments EBSD detector. Maps were collected at an accelerating voltage of 20 kV, with a step size provided in Supplementary Table 3, and the specimen tilted at 70°. Patterns were acquired with 4 × 4 binning and indexed using the Hough transform-based Tru-I indexing routine implemented in the AZtec software (version 5.0). The mean angular deviation (MAD) was calculated for each indexed point; the average MAD for the entire dataset was less than 0.45° provided in Supplementary Table 3. No data points were excluded based on MAD or other quality metrics. The overall indexing rates for EBSD characterizations at different temperatures are summarized in Supplementary Table 3.

Conventional transmission electron microscopy (TEM) and selected area electron diffraction (SAED) were carried out using a 200 kV field-emission TEM (TALOS F200X, Thermo Fisher Scientific, USA).

Temperature-dependent X-ray diffraction (XRD) patterns of the ZTE samples were recorded using a D/Max 2500PC diffractometer with monochromatic Cu Kα radiation (λ=1.5418 Å).

Mechanical properties and thermal expansion performance test

The dimension of the specimens for CTE measurement was Ø5 mm×3 mm. The linear thermal expansion data (dL/L) of samples were measured using a NETZSCH 402C Dilatometer under a heating rate of 5 ℃/min and temperature ranging from room temperature to 250 ℃. Cyclic thermal expansion tests were conducted over a temperature interval of 25 ℃ to 150 ℃ for a total of nine cycles. The room temperature compressive mechanical properties were measured by a CMT-5305-300 KN universal testing machine.

Calculations

Thermal stress and elastoplastic deformation generated between the particle and the matrix due to thermal mismatch were analyzed in this study using a model of a flat plate with a small hole [49-51]. At the initial temperature, the radius of the small hole in the matrix is equal to the particle radius. When the system cools to the target temperature, mutual constraint arises between the matrix and the particle because of the difference in their thermal expansion coefficients, leading to stress and strain in the matrix. The stress field resulting from the thermal expansion mismatch $(\alpha_m - \alpha_p)\Delta T$ was derived by solving the stress equilibrium and constitutive equations in spherical coordinates. Plastic yielding at the interface was determined using the von Mises criterion [52].:

$$(\sigma_e)_m = \frac{\sqrt{[(\sigma_r)_m - (\sigma_\theta)_m]^2 + [(\sigma_\theta)_m - (\sigma_\phi)_m]^2 + [(\sigma_\phi)_m - (\sigma_r)_m]^2}}{2} \quad (1)$$

This model provided the spatial stress distribution and the volume fraction of the plastically deformed zone.

The effective coefficient of thermal expansion (CTE) of the composite was calculated using a statistical ensemble method[53–55]. The matrix was treated as a system containing metastable, strained microstates. Their temperature-dependent probability $p^i(T)$ is governed by the partition function:

$$\rho^i = e^{\frac{G-G^i}{k_B T}} \tag{2}$$

Where $G^i(T)$ is the Gibbs free energy of state i, obtained via first-principles quasi-harmonic approximation (QHA) calculations. The system's CTE, is then a statistical average:

$$\left(\frac{\partial V}{\partial T}\right)_P = -\left(\frac{\partial S}{\partial P}\right)_T = \sum_{i=1}^{m}[\rho^i \frac{\partial V^i}{\partial T} + \frac{\partial P^i}{\partial T}(V^i - V^g)] \tag{3}$$

V_i and V_g are metastable state and steady state volume, respectively.

For more detailed analysis, please refer to the Supplementary Notes 1, 2 in the Supplementary Materials.

Data availability

All data supporting the findings of this study are included in the manuscript or the Supplementary Information. Source data are provided with this paper, and is available at the cited Figshare repository. [56]

References

1. Song, Y. *et al.* A lightweight shape-memory alloy with superior temperature-fluctuation resistance. *Nature* **638**, 965–971 (2025).
2. Xia, J. *et al.* Iron-based superelastic alloys with near-constant critical stress temperature dependence. *Science* **369**, 855–858 (2020).
3. Qiu, B. *et al.* Negative thermal expansion and oxygen-redox electrochemistry. *Nature* **640**, 941–946 (2025).
4. Kalaikkanal, K., Gobinath, N. & Mohan, R. Influence of swelling on the safety aspects of electric vehicle batteries – Short Review. *IOP Conf. Ser. Earth Environ. Sci.* **1161**, 012010 (2023).
5. Lohaus, S. H. *et al.* A thermodynamic explanation of the Invar effect. *Nat. Phys.* **19**, 1642–1648 (2023).
6. GUILLAUME, CH. ED. Invar and Its Applications. *Nature* **71**, 134–139 (1904).
7. Guillaume, Ch.-Éd. Recherches sur les aciers au nickel. *J. Phys. Théorique Appliquée* **7**, 262–274 (1898).
8. Ogawa, Y., Ando, D., Sutou, Y. & Koike, J. A lightweight shape-memory magnesium alloy. *Science* **353**, 368–370 (2016).
9. Yu-Hua, L., Xue, L. B., Xiao Bo, Z., Feng, Z. & Li-Li, J. Application of lightweight magnesium alloy in satellite antenna products. *J. Phys. Conf. Ser.* **1885**, 052001 (2021).
10. Wendt, D. *et al.* Entropic elasticity and negative thermal expansion in a simple cubic crystal. *Sci. Adv.* **5**, eaay2748 (2019).

11. van Schilfgaarde, M., Abrikosov, I. A. & Johansson, B. Origin of the Invar effect in iron–nickel alloys. *Nature* **400**, 46–49 (1999).
12. Aifantis, E. C. The physics of plastic deformation. *Int. J. Plast.* **3**, 211–247 (1987).
13. Valiev, R. Nanostructuring of metals by severe plastic deformation for advanced properties. *Nat. Mater.* **3**, 511–516 (2004).
14. Ahadi, A., Matsushita, Y., Sawaguchi, T., Sun, Q. P. & Tsuchiya, K. Origin of zero and negative thermal expansion in severely-deformed superelastic NiTi alloy. *Acta Mater.* **124**, 79–92 (2017).
15. Zhou, Y. *et al.* Residual stress regulation optimization of plastic and near-zero thermal expansion composite. *Acta Mater.* **288**, 120881 (2025).
16. Wei, X. & Kysar, J. W. Residual plastic strain recovery driven by grain boundary diffusion in nanocrystalline thin films. *Acta Mater.* **59**, 3937–3945 (2011).
17. Rajagopalan, J., Han, J. H. & Saif, M. T. A. Plastic Deformation Recovery in Freestanding Nanocrystalline Aluminum and Gold Thin Films. *Science* **315**, 1831–1834 (2007).
18. Vasil'yev, L. S. & Lomaev, S. L. Excess Volume in Materials with Dislocations. *Phys. Met. Metallogr.* **120**, 709–715 (2019).
19. Boleininger, M., Dudarev, S. L., Mason, D. R. & Martínez, E. Volume of a dislocation network. *Phys. Rev. Mater.* **6**, 063601 (2022).
20. Hayoune, A. & Hamana, D. A dilatometric and high-temperature X-ray diffraction study of cold deformation effect on the interaction between precipitation, recovery and recrystallization reactions in Al–12wt.% Mg alloy. *Mater. Sci. Eng. A* **527**, 7261–7264 (2010).
21. Gong, D. L. *et al.* Tuning thermal expansion by a continuing atomic rearrangement mechanism in a multifunctional titanium alloy. *J. Mater. Sci. Technol.* **80**, 234–243 (2021).
22. Iikubo, S. *et al.* Local Lattice Distortion in the Giant Negative Thermal Expansion Material Mn 3 Cu 1 − x Ge x N. *Phys. Rev. Lett.* **101**, 205901 (2008).
23. Li, Q., Zhu, H., Hu, L., Chen, J. & Xing, X. Negative Thermal Expansion in Nanosolids. *Acc. Chem. Res.* **52**, 2694–2702 (2019).
24. Eckart, C. The Thermodynamics of Irreversible Processes. IV. The Theory of Elasticity and Anelasticity. *Phys. Rev.* **73**, 373–382 (1948).
25. Chen, J.-H. *et al.* The influence of hydrostatic pressure and annealing conditions on the magnetostructural transitions in MnCoGe. *J. Appl. Phys.* **129**, 215108 (2021).
26. Noguchi, K. *et al.* Heat treatment effect on the magnetic properties and martensitic transformations of MnCoGe. *J. Magn. Magn. Mater.* **499**, 166199 (2020).

27. Zhao, Y.-Y. *et al.* Giant Negative Thermal Expansion in Bonded MnCoGe-Based Compounds with Ni_2In-Type Hexagonal Structure. *J. Am. Chem. Soc.* **137**, 1746–1749 (2015).
28. Liu, B.-Y. *et al.* Large plasticity in magnesium mediated by pyramidal dislocations. *Science* **365**, 73–75 (2019).
29. Zhang, C., Zhang, Z., Wang, D. & Hu, Y. Magnetic phase transition and magnetocaloric effect in hexagonal MnCoGe alloys mediated by axial strain: a Monte Carlo study. *Phys. Chem. Chem. Phys.* **27**, 2046–2052 (2025).
30. Ganeshan, S., Shang, S. L., Wang, Y. & Liu, Z.-K. Effect of alloying elements on the elastic properties of Mg from first-principles calculations. *Acta Mater.* **57**, 3876–3884 (2009).
31. Zhou, C. *et al.* High-performance zero thermal expansion in Al metal matrix composites. *Acta Mater.* **275**, 120076 (2024).
32. Zhou, C., Zhang, Q., Liu, Y., Wu, G. & Liu, S. Thermal expansion of $Y_2W_3O_{12}$ /Al metal matrix composites. *Mater. Res. Innov.* **18**, S4-490-S4-494 (2014).
33. Takenaka, K., Otsuka, K., Okamoto, Y., Kume, Y. & Kobashi, M. Fabrication of Metal Matrix Composite Containing Manganese Nitride Showing Giant Negative Thermal Expansion by Compressive Torsion Processing. *Mater. Trans.* **62**, 590–595 (2021).
34. Zhou, C. *et al.* Lightweight and near-zero thermal expansion ZrW2O8-SiCnw/Al hybrid composites. *J. Alloys Compd.* **907**, 164444 (2022).
35. Yang, J. *et al.* Effect of sintering temperature on the thermal expansion behavior of $ZrMgMo_3\ O_{12p}$/2024Al composite. *Ceram. Int.* **44**, 10744–10752 (2018).
36. Zhou, Y. *et al.* The effect of interface reaction on the thermal and mechanical properties of Mn3.2Zn0.5Sn0.3N/Al composites. *Ceram. Int.* **48**, 25826–25832 (2022).
37. Sheng, J. *et al.* Thermal expansion behavior of copper matrix composite containing negative thermal expansion $PbTiO_3$ particles. *Mater. Des.* **132**, 442–447 (2017).
38. Holzer, H. & Dunand, D. C. Phase transformation and thermal expansion of Cu/ZrW_2O_8 metal matrix composites. *J. Mater. Res.* **14**, 780–789 (1999).
39. Wang, Q., Dong, Y., Jiang, Z. & Huang, J. Enhancing low thermal expansion behavior and strength via induced Zr-rich intermetallic phase in Fe-36Ni Invar alloy. *Mater. Des.* **226**, 111644 (2023).
40. Zhou, Y. *et al.* Sintering Temperature Effect of Near-Zero Thermal Expansion $Mn_3Zn_{0.8}Sn_{0.2}N$/Ti Composites. *Materials* **16**, 5919 (2023).
41. Wu, S. *et al.* Tuning the thermal expansion behavior and promoting the mechanical properties of Mg–9Al–1Zn magnesium alloys by the introduction of MnCoGe-based alloys. *Scr. Mater.* **214**, 114680 (2022).

42. Huang, Y. *et al.* Localized magnetic moments variation for strengthening and tuning thermal expansion behavior of Mg alloys. *Acta Mater.* **259**, 119238 (2023).
43. Ateba Betanda, Y. *et al.* Measurement of stored energy in Fe–48%Ni alloys strongly cold-rolled using three approaches: Neutron diffraction, Dillamore and KAM approaches. *Mater. Sci. Eng. A* **614**, 193–198 (2014).
44. Aly, K. A., Khalil, N. M., Algamal, Y. & Saleem, Q. M. A. Estimation of lattice strain for zirconia nano-particles based on Williamson- Hall analysis. *Mater. Chem. Phys.* **193**, 182–188 (2017).
45. Wang, J. *et al.* Outstanding mechanical and magnetocaloric properties of MnCoGe alloy fabricated through hot pressing sintering. *J. Mater. Res. Technol.* **33**, 8611–8617 (2024).
46. Xiong, Y. *et al.* Atomistic studies of the responses of composites with thermal residual stresses and defects under uniaxial loading. *J. Alloys Compd.* **901**, 163664 (2022).
47. Zhou, Y. C., Long, S. G., Duan, Z. P. & Hashida, T. Thermal Damage in Particulate-Reinforced Metal Matrix Composites. *J. Eng. Mater. Technol.* **123**, 251–260 (2001).
48. Ibrahim, I. A., Mohamed, F. A. & Lavernia, E. J. Particulate reinforced metal matrix composites — a review. *J. Mater. Sci.* **26**, 1137–1156 (1991).
49. Meijer, G., Ellyin, F. & Xia, Z. Aspects of residual thermal stress/strain in particle reinforced metal matrix composites. *Compos. Part B Eng.* **31**, 29–37 (2000).
50. Elomari, S., Skibo, M. D., Sundarrajan, A. & Richards, H. Thermal expansion behavior of particulate metal-matrix composites. *Compos. Sci. Technol.* **58**, 369–376 (1998).
51. Wong, C. S., Pramanik, A. & Basak, A. K. Residual stress generation in metal matrix composites after cooling. *Mater. Sci. Technol.* **34**, 1388–1400 (2018).
52. Davis, L. C. Flow rule for the plastic deformation of particiulate metal-matrix composites. *Comput. Mater. Sci.* **6**, 310–318 (1996).
53. Liu, Z.-K. On Gibbs Equilibrium and Hillert Nonequilibrium Thermodynamics. *J. Phase Equilibria Diffus.* **45**, 965–985 (2024).
54. Hew, N. L. E., Shang, S.-L. & Liu, Z.-K. Predicting phase transitions in $PbTiO_3$ using zentropy through quasiharmonic phonon calculations. *Phys. Rev. B* **110**, 184103 (2024).
55. Liu, Z.-K. Quantitative predictive theories through integrating quantum, statistical, equilibrium, and nonequilibrium thermodynamics. *J. Phys. Condens. Matter* **36**, 343003 (2024).
56. A lightweight zero thermal expansion magnesium alloy. (2026). [Figshare Data set]. https://doi.org/10.6084/m9.figshare.31331044

Acknowledgements

We thank Ying Sun (Beihang University), Kun Lin (University of Science and Technology Beijing) for assistance with the CTE data interpretation; Yu Zhang, Liang Yu, Chunhua Ran, Yuyang Gao, Sixue Qin (Chongqing University) for their help on characterization and discussion of the microstructure and properties of the sample. It was also getting support from Sinoma Institute of Materials Research (Guang Zhou) Co., Ltd (SIMR).

This work was supported by the National Key Research and Development Program of China (No. 2022YFB3709300 and 2021YFB3701000 for B. J.), the National Natural Science Foundation of China (No. 52571125 for S. W., U21A2048 and U2037601 for B. J.), the Fundamental Research Funds for the Central Universities (No. 2024CDJCGJ-009 and 2024CDJYXTD-002 for B. J.) and National Natural Science Foundation of China Youth Fund (No. 12204254 for Z. D.).

Author contributions Statement

S. W and Y. H developed the concept and wrote the first draft of the manuscript. Z. D, J. S, G. W, C. W, S. B, P. B, B. J, F. P wrote the final draft of the manuscript. All authors were involved in discussions and evaluation of drafts during the writing process. S. W, G. W. and B. J. directed the research.

Competing interests Statement

The authors declare no competing interests.

Figure Legends/Captions

Figure 1 Schematic illustration the strain recovery complementary strategy and the characterization of the strain. a, Schematic diagram depicting the concept of strain recovery. In the strain recovery stage, the macroscopic volume change (ΔV) over a specific temperature range (ΔT) can approach zero, as the volume/length variation induced by thermal expansion is persistently offset by the release of stored internal strain. This process primarily involves the dissipation or redistribution of thermal energy among various defect types, minimizing macroscopic volume expansion. Upon cooling, the significant volume expansion of the particles due to phase transformation, along with the subsequent unmatched contraction, initiates the reestablishment of strain in the Mg matrix. The axes are conceptual and not to scale; low/high temperatures represent relative endpoints of the thermal cycle. Color gradients within grains (indicating matrix strain) are qualitative indicators of strain evolution (white: low strain, red: high strain). **b-e,** EBSD orientation maps and KAM diagrams illustrating the strain distribution in the ZTE alloy compared to the WE43

Mg alloy. **f-g**, HRTEM images detail the dislocation arrays and lattice distortion of Mg matrix close to the MnCoGe particles. **h**, SAED pattern of the MnCoGe region in **g**. **i–j**, HRTEM images of the Mg matrix indicated by the orange and green boxes in **g**, with lattice fringe measurements labeled.

Figure 2 Thermal expansion and mechanical properties. a, Thermal expansion curves comparing pure WE43 and the ZTE sample at room temperature, highlighting the near-zero thermal expansion behavior. **b**, Compressive stress-strain curves of the WE43 and ZTE sample at room temperature, demonstrating its mechanical performance. **c**, Thermal expansion curves of the ZTE sample over nine cycles from RT to 150 °C. **d**, Average CTE values obtained from the nine-cycle thermal expansion tests. **e-f**, Comparative overview of the logarithmic CTE (Lg (CTE)), temperature range, and density for previously reported alloys, intermetallic compounds, and composite systems exhibiting ZTE behavior. Source data for (a-f) are provided as a Source data file.

Figure 3 Tracking strain evolution during temperature cycling. a, In-situ EBSD images of the ZTE sample processed by heating to 300 °C and cooling to 25 °C, showing the distributions of a grain-scaled morphology and orientation. **b**, KAM images display the strain evolution during temperature cycling. The appearance of distinct color contrast indicates significant strain, whereas a reduction in contrast suggests a decrease in strain. **c**, Average geometrically necessary dislocation (GND) density at different temperatures. GND density was calculated from KAM values obtained via EBSD analysis. Mean values were derived from statistical histograms of GND distribution. Data are presented as mean ± standard error of the mean (error bars). Detailed statistics, including total pixel counts for each condition, are provided in Supplementary Table 4. **d**, Stored energy calculated via the KAM approach, based on local misorientation from EBSD data to estimate GND density. **e**, In-situ XRD show that the evolution of lattice parameters of Mg during heating and cooling. **f**, The variation of strain on the Mg matrix as a function of temperature. Source data for (c-f) are provided as a Source data file.

Figure 4 The contribution of stain recovery on thermal expansion. a, DSC curves for the ZTE sample during thermal cycling. **b**, Comparative DSC curves of the ZTE sample, MnCoGe and the WE43 alloy. The MnCoGe phase transformation is characterized by an endothermic process during heating. In contrast, the ZTE sample shows exothermic peaks during both heating and cooling, indicating the different energy transition mechanisms between MnCoGe and ZTE sample. **c**, The volume changes in the Mg unit cell under varying strain conditions along the c-axis. **d**, Temperature-dependent evolution and statistical probabilities of microscopic strain in Mg matrix, with stress applied along the [0001] and $[2\bar{1}\bar{1}0]$ crystallographic directions. **e**, Comparative analysis of calculated and experimental CTE, demonstrating the major contribution of compressive stain. Source data for (a-e) are provided as a Source data file.

Editor's Summary

This work demonstrates that embedding MnCoGe particles within magnesium alloys transforms the irreversible thermal expansion into a self-compensating behavior, yielding zero thermal expansion from 25 to 150 °C while retaining high strength and ultralow density.

Peer review information: *Nature Communications* thanks Gangjian Tan and the other, anonymous, reviewer(s) for their contribution to the peer review of this work. A peer review file is available.

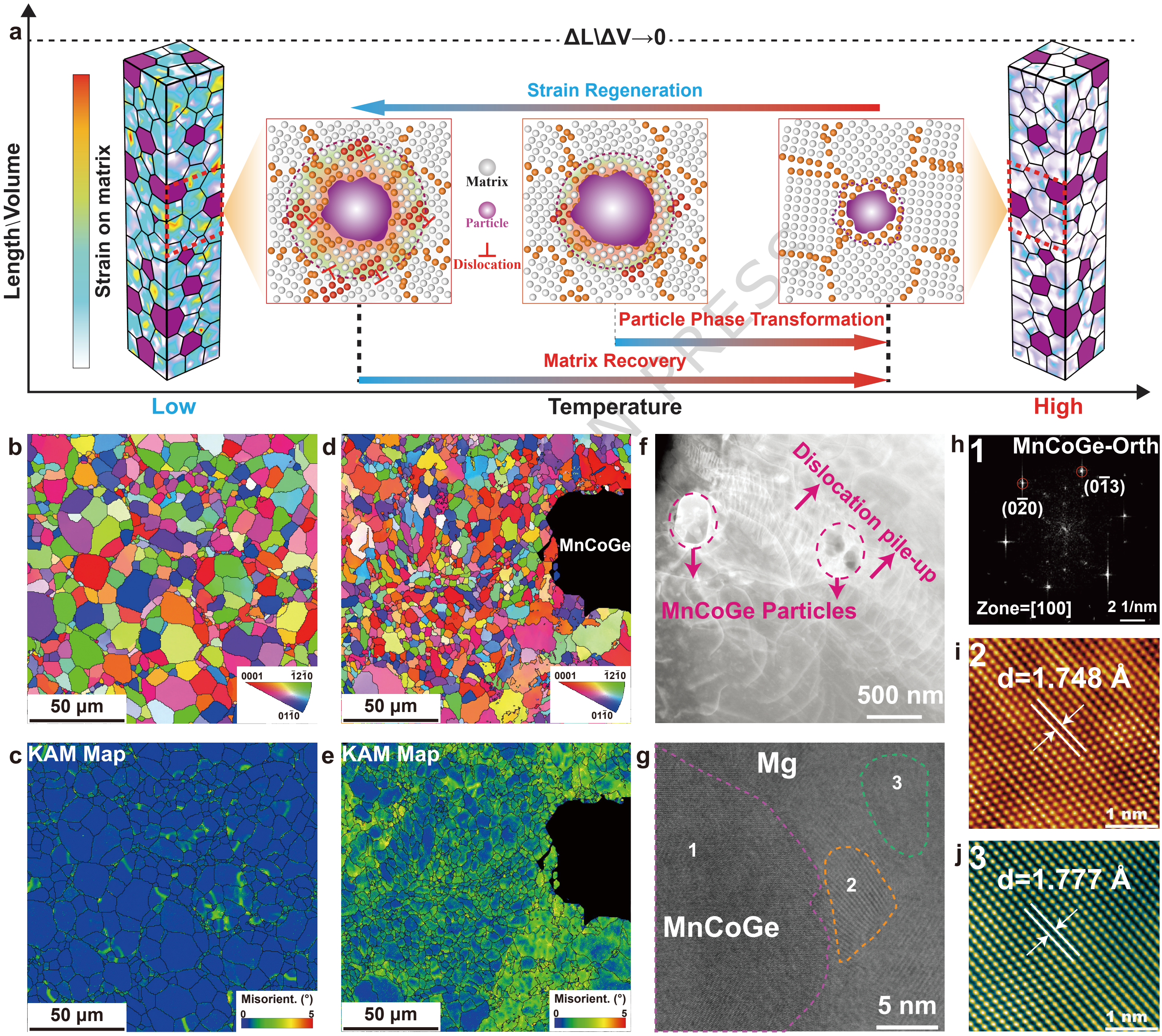
a
ΔL\ΔV→0
Length\Volume
Strain on matrix
Strain Regeneration
Matrix
Particle
⊥
Dislocation
Particle Phase Transformation
Matrix Recovery
Low
Temperature
High
b
50 μm
0001
1̄21̄0
011̄0
c
KAM Map
50 μm
Misorient. (°)
0
5
d
MnCoGe
50 μm
0001
1̄21̄0
011̄0
e
KAM Map
50 μm
Misorient. (°)
0
5
f
Dislocation pile-up
MnCoGe Particles
500 nm
g
Mg
1
2
3
MnCoGe
5 nm
h
1
MnCoGe-Orth
(01̄3)
(02̄0)
Zone=[100]
2 1/nm
i
2
d=1.748 Å
1 nm
j
3
d=1.777 Å
1 nm

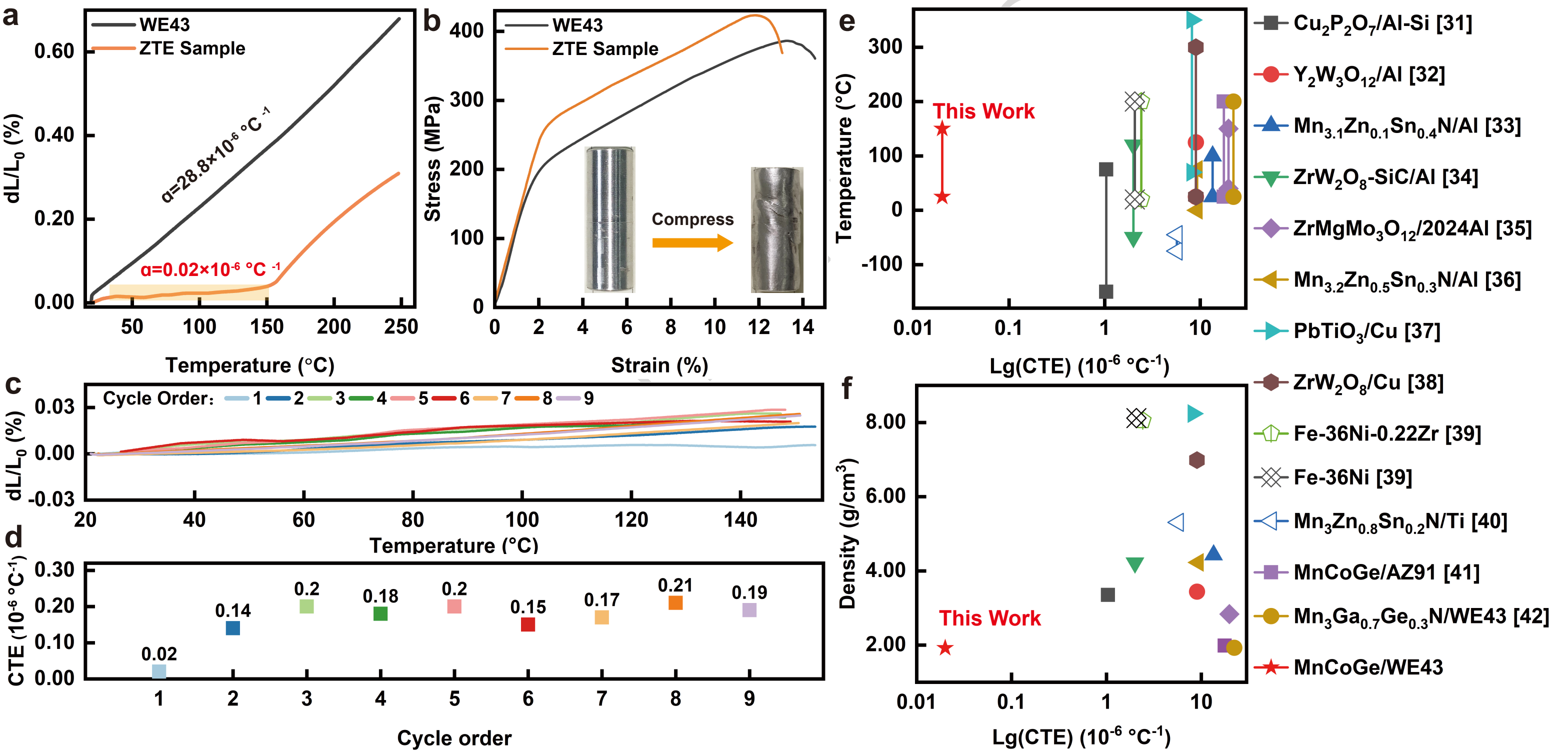
a
WE43
ZTE Sample
α=28.8×10-6 °C -1
α=0.02×10-6 °C -1
dL/L0 (%)
0.60
0.40
0.20
0.00
50
100
150
200
250
Temperature (°C)
b
WE43
ZTE Sample
Compress
Stress (MPa)
400
300
200
100
0
0
2
4
6
8
10
12
14
Strain (%)
c
Cycle Order: 1 2 3 4 5 6 7 8 9
dL/L0 (%)
0.03
0.00
-0.03
20
40
60
80
100
120
140
Temperature (°C)
d
CTE (10-6 °C-1)
0.30
0.20
0.10
0.00
0.02
0.14
0.2
0.18
0.2
0.15
0.17
0.21
0.19
1
2
3
4
5
6
7
8
9
Cycle order
e
This Work
Temperature (°C)
300
200
100
0
-100
0.01
0.1
1
10
Lg(CTE) (10-6 °C-1)
f
This Work
Density (g/cm3)
8.00
6.00
4.00
2.00
0.01
0.1
1
10
Lg(CTE) (10-6 °C-1)
Cu2P2O7/Al-Si [31]
Y2W3O12/Al [32]
Mn3.1Zn0.1Sn0.4N/Al [33]
ZrW2O8-SiC/Al [34]
ZrMgMo3O12/2024Al [35]
Mn3.2Zn0.5Sn0.3N/Al [36]
PbTiO3/Cu [37]
ZrW2O8/Cu [38]
Fe-36Ni-0.22Zr [39]
Fe-36Ni [39]
Mn3Zn0.8Sn0.2N/Ti [40]
MnCoGe/AZ91 [41]
Mn3Ga0.7Ge0.3N/WE43 [42]
MnCoGe/WE43

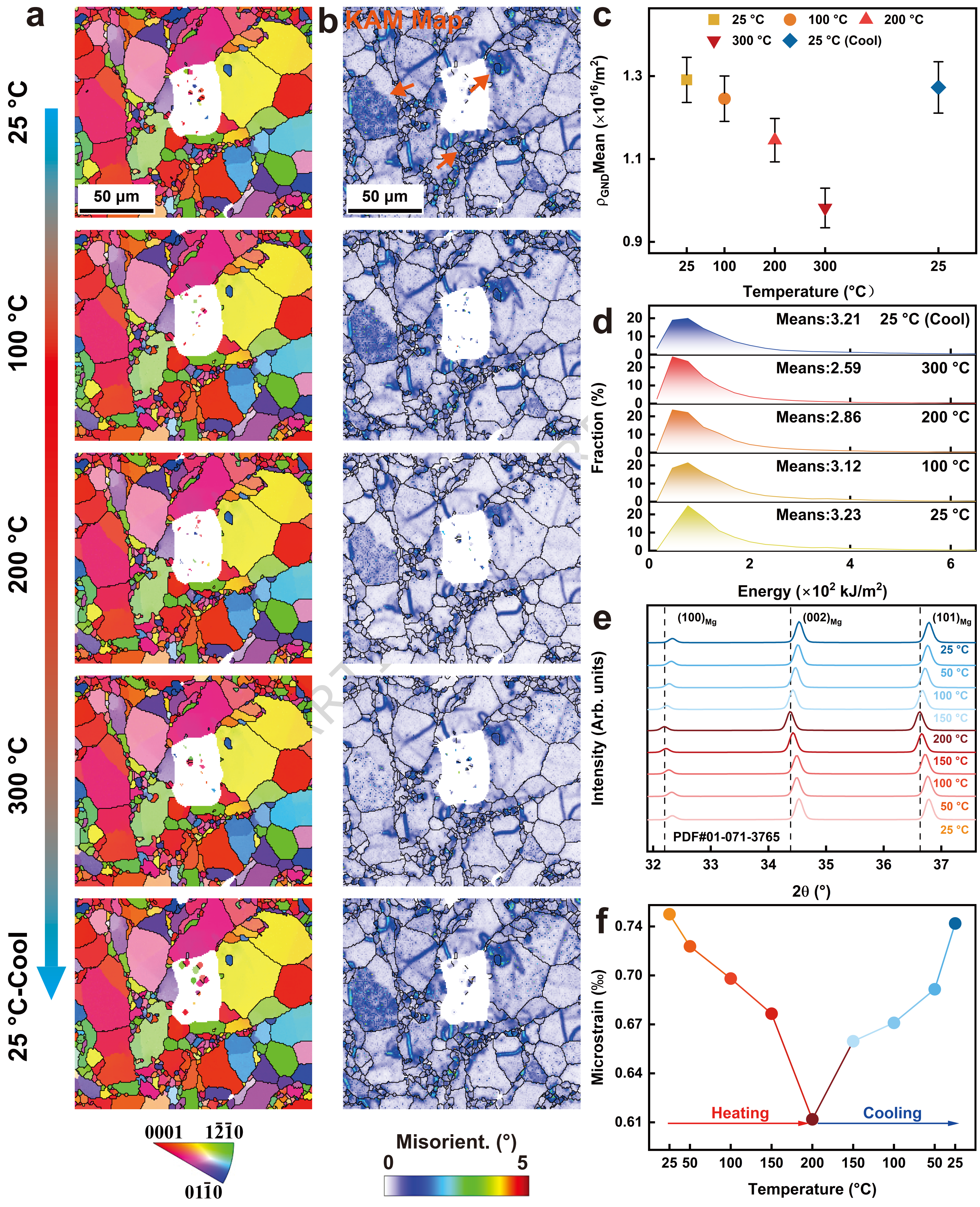
a
b
KAM Map
c
d
e
f
25 °C
100 °C
200 °C
300 °C
25 °C-Cool
50 μm
50 μm
0001
1$\bar{2}\bar{1}$0
01$\bar{1}$0
Misorient. (°)
0
5
25 °C
100 °C
200 °C
300 °C
25 °C (Cool)
ρ_{GND}Mean ($\times10^{16}/m^2$)
1.3
1.1
0.9
25
100
200
300
25
Temperature (°C)
Means:3.21
25 °C (Cool)
Means:2.59
300 °C
Means:2.86
200 °C
Means:3.12
100 °C
Means:3.23
25 °C
Fraction (%)
20
10
0
0
2
4
6
Energy ($\times10^2$ kJ/m^2)
$(100)_{Mg}$
$(002)_{Mg}$
$(101)_{Mg}$
25 °C
50 °C
100 °C
150 °C
200 °C
150 °C
100 °C
50 °C
25 °C
PDF#01-071-3765
Intensity (Arb. units)
32
33
34
35
36
37
2θ (°)
Microstrain (‰)
0.74
0.70
0.67
0.64
0.61
Heating
Cooling
25
50
100
150
200
150
100
50
25
Temperature (°C)

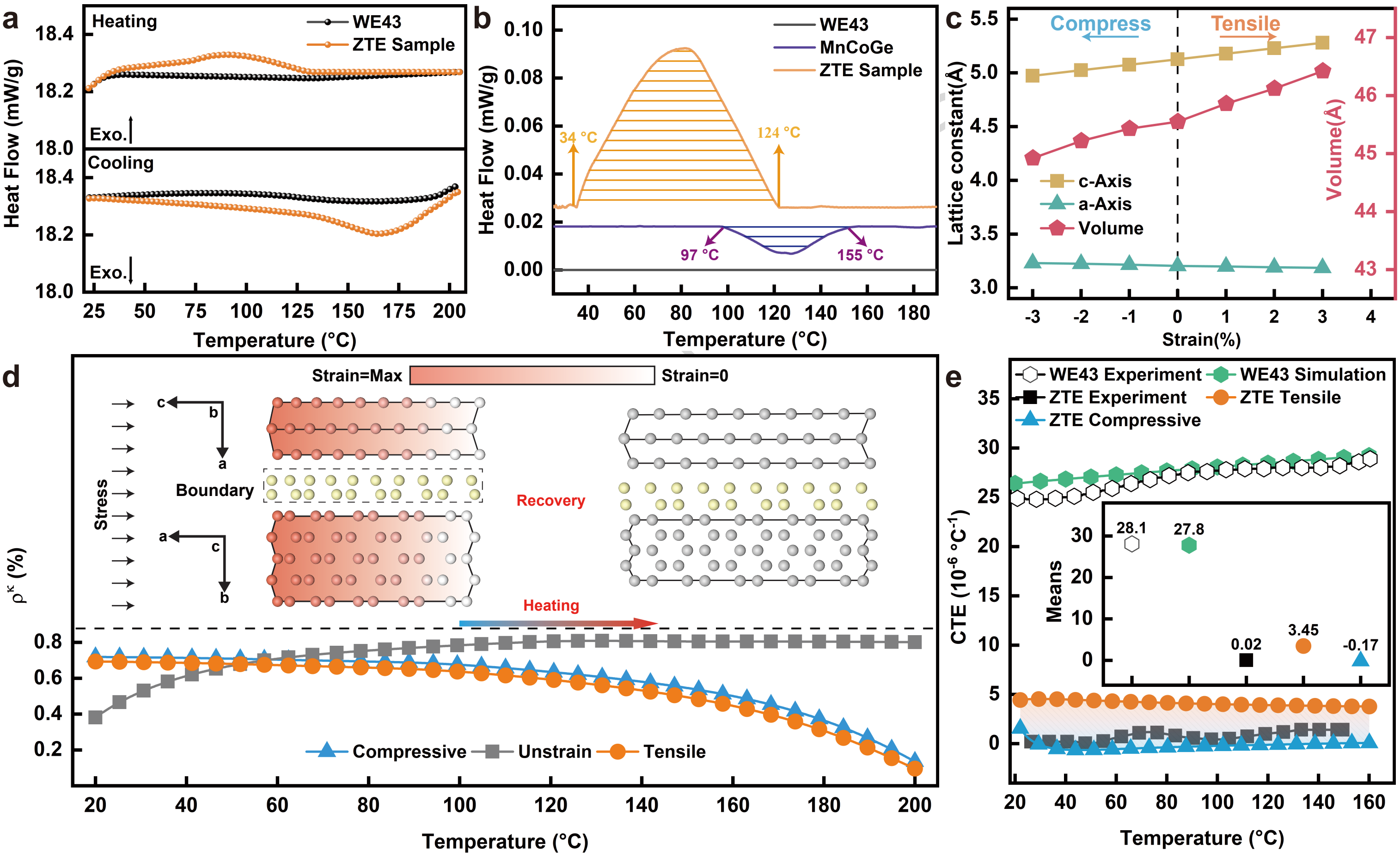
a
Heating
WE43
ZTE Sample
Exo.
Cooling
Exo.
Heat Flow (mW/g)
18.4
18.2
18.0
25
50
75
100
125
150
175
200
Temperature (°C)
b
WE43
MnCoGe
ZTE Sample
34 °C
124 °C
97 °C
155 °C
Heat Flow (mW/g)
0.10
0.08
0.06
0.04
0.02
0.00
40
60
80
100
120
140
160
180
Temperature (°C)
c
Compress
Tensile
c-Axis
a-Axis
Volume
Lattice constant(Å)
Volume(Å)
5.5
5.0
4.5
4.0
3.5
3.0
47
46
45
44
43
-3
-2
-1
0
1
2
3
4
Strain(%)
d
Strain=Max
Strain=0
Stress
c
b
a
Boundary
a
c
b
Recovery
Heating
ρ^κ (%)
0.8
0.6
0.4
0.2
Compressive
Unstrain
Tensile
20
40
60
80
100
120
140
160
180
200
Temperature (°C)
e
WE43 Experiment
WE43 Simulation
ZTE Experiment
ZTE Tensile
ZTE Compressive
CTE (10^-6 °C^-1)
35
30
25
20
15
10
5
0
Means
30
20
10
0
28.1
27.8
0.02
3.45
-0.17
20
40
60
80
100
120
140
160
Temperature (°C)